RESEARCH PAPER

Towards real-time monitoring of metal transfer and melt pool temperature field in gas metal arc directed energy deposition

Prashant Kumar Chaurasia[1] · Sven Frithjof Goecke[2] · Amitava De[1]

Abstract

Large three-dimensional metallic parts can be printed layer-by-layer using gas metal arc directed energy deposition (GMA-DED) process at a high deposition rate and with little or no material wastage. Fast responsive real-time monitoring of GMA-DED process signatures and their transient variations is required for printing of dimensionally accurate and structurally sound parts. A systematic experimental investigation is presented here on multi-layer GMA-DED with two different scanning strategies using a high strength low alloy (HSLA) filler wire. The dynamic metal transfer, melt pool temperature field and its longitudinal cross-section, and arc voltage and current are monitored synchronously. The transient arc heat input and the melt pool solidification cooling rate are estimated from the monitored signals. The layer-wise variations of the melt pool dimension, surface temperature profile, thermal cycles, and solidification cooling rate are examined for different scanning strategies. It is comprehended that the part defects can be minimized, and the mass production of zero-defect parts can be achieved in GMA-DED process with synchronized monitoring and assessment of the real-time process signatures.

1 Introduction

A metallic filler wire feedstock is melted and deposited along multiple tracks and layers for layer-by-layer printing of large three-dimensional (3D) part in GMA-DED [1–7]. An appropriate control of the important variables such as scanning strategy, printing travel speed (PTS), and wire feed rate (WFR), and an understanding of their effects on the real-time process signatures are needed to print dimensionally consistent and defect-free parts in GMA-DED [3–7]. The real-time monitoring of process signatures can enhance the process efficiency and deposition quality in GMA-DED and systematic investigations in this direction are currently emerging [6–8].

The real-time probing of temperature field [9], melt pool boundary [10], weld seam offset [11], and weld defects [12] are vastly reported for arc welding [9–14]. Similar efforts are recently started for wire arc additive manufacturing (AM) processes [5–8]. For example, a thermal camera was used to capture the real-time temperature field in melt pool for GMA-DED [7–9]. Mathieu et al. [15] used a mono-colour infrared (IR) camera for monitoring of thermal cycles for laser brazing of multi-material assembly. Yang et al. [6] and Rodrigues et al. [5] also used IR mono-colour camera for probing melt pool temperature field in real-time for GMA-DED considering a fixed calibration factor to convert the recorded radiating intensity values into corresponding temperature. In contrast to a mono-colour camera, a two-colour camera can provide the actual temperature field regardless of the variation in the emissivity values within a narrow range of wavelengths [14–20]. The use of two-colour camera has started for monitoring of real-time temperature field for GMA-DED [7, 8] and gas metal arc (GMA) brazing [9].

✉ Prashant Kumar Chaurasia
   prashant9161@gmail.com

   Sven Frithjof Goecke
   goecke@th-brandenburg.de

   Amitava De
   amit@iitb.ac.in

[1] Indian Institute of Technology Bombay, Mumbai 400076, India

[2] University of Applied Science, 14770 Brandenburg an der Havel, Germany

The metal transfer characteristics from filler wire commonly provided a measure of the process stability for arc welding [21–25], gas tungsten arc directed energy deposition (GTA-DED) [26], and GMA-DED [27, 28]. Hermans et al. [21] used a high-speed video camera to monitor the dynamic metal transfer and melt pool stability for GMAW at a sampling rate of 4 kHz and reported the enhanced process stability when the short-circuiting frequency was equal to the oscillation frequency of the melt pool. A synchronized monitoring of current and voltage transients at a sampling rate of 20 kHz, and of metal transfer at a sampling rate of 5 kHz was used by Ersoy et al. [22] and Santos et al. [23] to visualize the droplet formation and transfer through the arc plasma [23] and spatter generation due to arc start instability for pulse current GMAW [22]. In a similar study, Johnson et al. [24] and Zou et al. [25] also used the high-speed camera for GMAW [24] and GTAW [25] processes to visualize the different modes of metal transfer. Wu et al. [26] also used a similar high-speed camera to view the metal transfer and arc length for GTA-DED at a sampling rate of 1 kHz and observed a gradual change from bridge transfer to interrupted metal transfer as the deposition moved to the upper layers. Cadiou et al. [28] used a high-speed camera for real-time monitoring of melt pool depth and length from the longitudinal view of the melt pool images during GMA-DED at a sampling rate of 2 kHz. These studies show that the real-time monitoring of the dynamic metal transfer and melt pool are required for an insightful understanding of the electric arc assisted DED processes.

The aforementioned investigations illustrate that the transient process signatures such as metal transfer, melt pool temperature field, and arc power can provide an important quantitative knowledge on the impending quality of the printed parts in GMA-DED. Investigations on real-time monitoring of process transients have recently begun for GMA-DED [7] and further detail studies are clearly needed due to the complex nature of the process. A detailed investigation is therefore undertaken in the present work towards the real-time monitoring of multi-layer GMA-DED with unidirectional and bidirectional scanning. The effects of the scanning strategies on the metal transfer characteristics, melt pool temperature field and its longitudinal cross-sections, and thermal cycles are examined thoroughly for unidirectional and bidirectional scanning.

2 Experimental details

Figure 1a presents the GMA-DED set-up and the real-time monitoring apparatus which are used in the present work [7]. An advanced GMA welding power source with a reversed wire feed technology (Fronius VR 7000 CMT) was integrated with a six-axis FANUC robot. The scanning trajectory and the printing travel speed were pre-programmed for the wire feeder using a FANUC controller. The wire feeder unit was set perpendicular to the fixed worktable (x-y plane) and moved along x-axis, the deposition direction (Fig. 1a). A fast responsive transient data recorder (DEWE 2-A4-32) was used for synchronous monitoring of arc voltage and current in real-time at 5 kHz sampling frequency. Two mono-colour IR and one two-colour quotient thermal camera were fixed with the wire feeder unit to record the real-time temperature field of melt pool and the adjoining trailing solidified region. One video camera with high-speed recording capacity was fixed perpendicular to both the deposition direction and the wire feeder unit to capture the evolution of the melt

Fig. 1 **a** GMA-DED set-up with recording instrumentations [(1) two-colour (TC) and (2, 3) mono-colour (MC-1, MC-2) thermal cameras, (4) process cabin, (5) wire feeding unit, (6) six-axis FANUC robot, (7) video camera, (8) baseplate] [7], and illustration of **b** unidirectional and **c** bidirectional scanning
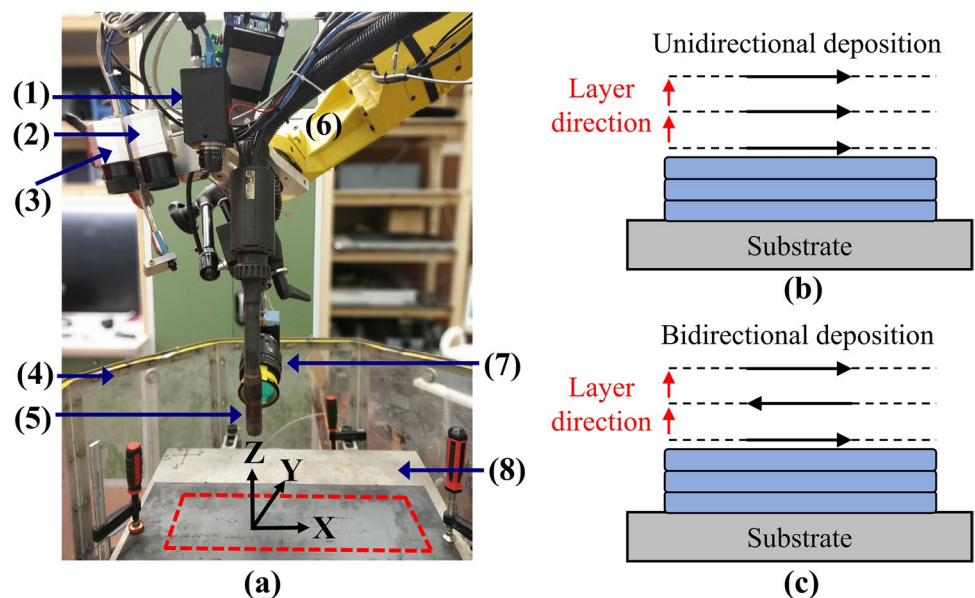
pool and the metal transfer longitudinally (x-z plane). The detailed specifications of the video camera and the IR thermal camera are already presented in reference [7] and are not repeated here.

Figure 1b–c illustrate unidirectional and bidirectional scanning strategies for the single-track multi-layer GMA-DED. In unidirectional scanning strategy, the start and end positions are fixed for each layer and the wire feeder unit moves in the same deposition direction for printing all the layers (Fig. 1b). In contrast, the start and the end positions are interchanged for the printing of alternate layers in case of the bidirectional scanning strategy (Fig. 1c). The sample deposits were made using a 1.2 mm diameter HSLA (Union NiMoCr) filler wire on a steel (S690) substrate with a WFR of 6 m/min and PTS of 6 mm/s. The S690 substrate confirms to a fine-grained steel which is used for structural fabrications [7]. The Union NiMoCr HSLA filler wire specification confirms to AWS A5.28 ER100S-G [7]. The length, width, and height of the substrate were 90 mm, 80 mm, and 25 mm, respectively. The track length of all the builds was kept fixed as 50 mm. Once the deposition of a layer along a track is completed, the welding torch along with the thermal cameras is kept stationary at the end of the track. The thermal cameras continue to monitor the temperature of the top surface at the end of the track till the temperature there cools down to the pre-set interpass temperature, 423 K. It is presumed that once the temperature at the end of the track cools down to 423 K, the rest of the track will eventually attain a temperature 423 K or lower. The mono-colour IR thermal camera (MC-2), in particular, is used to monitor the cooling down of the top surface at the end of the track

since MC-2 is capable of measuring a temperature range of 423–1173 K. The distance between the contact tip to the depositing surface was kept equal to 15 mm. An Ar-18%CO_2 gas mixture (ISO14175:M21) was used for shielding at a flow rate of 15 L/min. The baseplate was clamped at all the four corners with the worktable shown in Fig. 1a.

3 Results and discussion

3.1 Monitoring metal transfer, and arc voltage and current

Figure 2a–b show a synchronous recording of the transient voltage and current signals, and the longitudinal (in x-z plane) melt pool view for printing of a typical ninth layer for a ten-layer sample. The time-averaged arc power and heat input per unit length are obtained from the transient voltage and current signals as 3.14 kW and 461.04 J/mm, respectively. The time-averaged arc power (P) is estimated as a weighted average of the product of the recorded real-time current and voltage values over arcing and short-circuiting phases for a current/voltage cycle. For a specific WFR, the time-averaged arc power (P) is estimated for ten current/voltage cycles, and an average value is considered. The heat input per unit length (q) is calculated as ($\eta P/v$) where v is the PTS and η is the process efficiency, which is assumed to be 0.88 [29, 30]. Further details on the estimation of arc power and heat input per unit length from the recorded current voltage transients are presented in reference [7, 9] and are not repeated here. The current and voltage cycles include

Fig. 2 **a** Measured current and voltage transients for 6 m/min wire feed rate [7], **b** a melt pool longitudinal section from high-speed video camera along ninth layer for unidirectional scanning, and **c** sequential melt pool longitudinal sections from *I*st to *V*th time instants (please refer to Fig. 2a) along ninth layer for unidirectional and bidirectional scanning
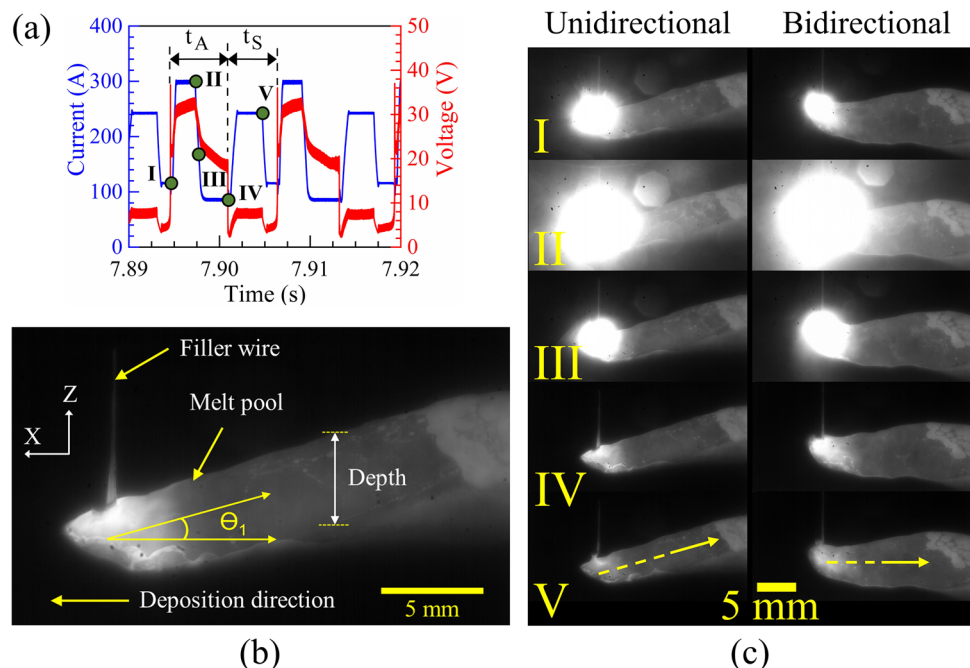
an arcing (t_A) phase and a short-circuiting phase (t_S), which are broadly realized through five successive instants (*I* to *V*). A low-power arc ignites at the onset of the arcing phase at a low current at the time instant *I* and the instantaneous current reaches at its maximum at the time instant *II* resulting in an enlarged arc (Fig. 2a, c) and faster melting of the filler wire. The instant *III* presents a testimony of a smooth reduction of current and voltage and a controlled end of the arcing phase followed by the onset of the short-circuiting phase as the molten metal at the tip of the filler touches the melt pool in the baseplate or previous deposit (instant *IV*). A liquid bridge is formed and the arc is almost non-existent at this stage. The time instant *V* exhibits an instantaneous high current that helps in pinching and shearing of the liquid metal from the filler wire. The reversed wire feed technology of the power source also helps in sharing of the liquid bridge [27].

Figure 2c shows the sequence of metal transfer through the five time instants, *I* to *V*, which are shown in Fig. 2a, for both unidirectional and bidirectional scanning strategies. The melt pools for the unidirectional scanning strategy in Fig. 2c show a little inclined elevation as compared to that for the bidirectional scanning strategy. This is attributed to the greater height of solidified material at the start position for the unidirectional scanning strategy. The melt pool elevation is measured in terms of the inclination angle (θ_I) with

respect to the deposition direction as shown in Fig. 2b. The average depth and elevation of the melt pool are measured as 6.5 ($\pm$0.3) mm and 15.91° ($\pm$0.25), respectively. A comparison of the melt pool images at the respective time instants for unidirectional and bidirectional scanning strategies in Fig. 2c indicates a slight increase in the melt pool depth in the latter case, which is attributed to the relatively straight longitudinal profile of the melt pool. The average melt pool depth during bidirectional deposition in Fig. 2c is around 7.1 ($\pm$0.4) mm.

3.2 Monitoring of surface temperature field

Figure 3 shows the temperature field of the top surface, including melt pool and the adjacent trailing solidified region for the second, sixth, and ninth layers from two-colour and mono-colour thermal cameras. The grey coloured region at the beginning in each figure represents a little blockage of the camera view by the gas nozzle, which could not be avoided for adjusting multiple cameras in a small region. In Fig. 3a–l, the region heated beyond the liquidus temperature (1812 K) of HSLA filler wire is considered to be the molten region.

Figure 3a–c show that the pool length increases consistently from the second to the ninth layer for unidirectional scanning. This is attributed to accumulation of heat in the build wall as the deposition moves to upper layers
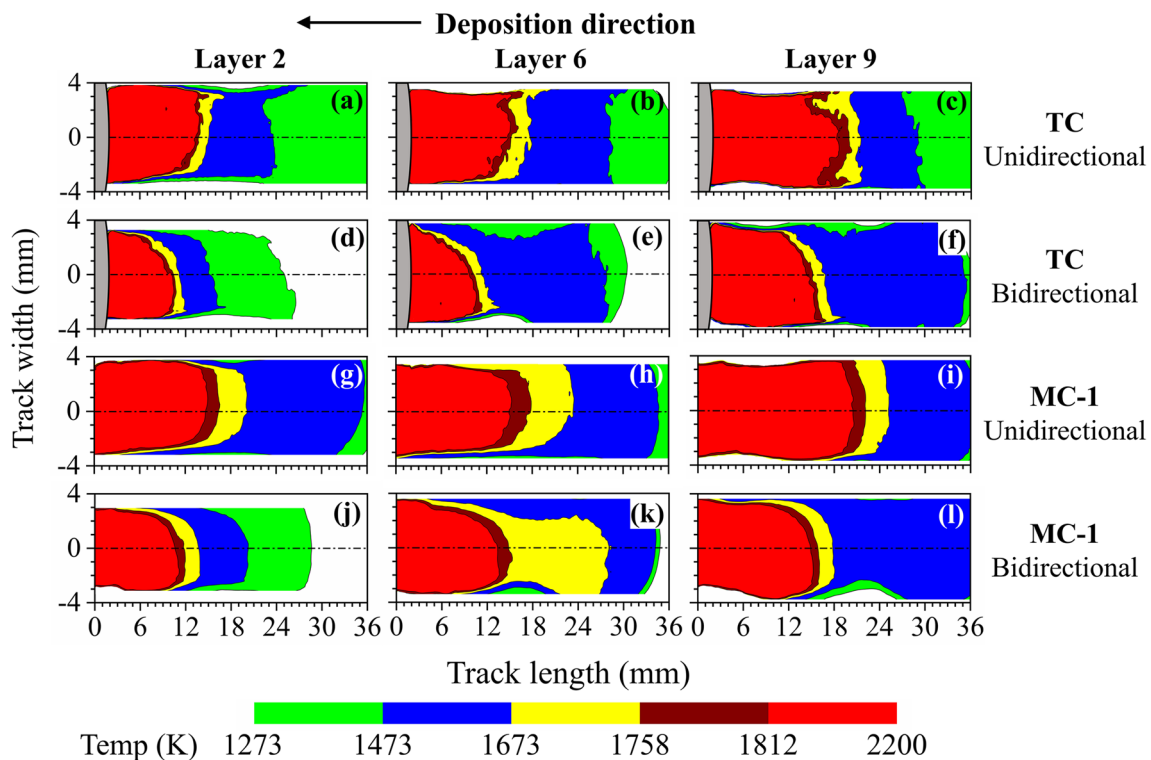
Fig. 3 Recorded temperature field of the top surface, including melt pool and the adjacent trailing solidified region, for the second, sixth, and ninth layers from two-colour (TC) and mono-colour (MC-1) thermal cameras for unidirectional and bidirectional scanning

and consequent decrease in the rate of heat loss through the wall. A similar increase, albeit to a smaller extent, in the pool length from the first to the ninth layer is also noted for the bidirectional scanning in Fig. 3d–f. The smaller change in the pool length from the lower to the upper layers for the bidirectional scanning is attributed to an even distribution of heat accumulation along the length of the deposited wall.

The mono-colour thermal camera uses a single emissivity-based conversion factor to calibrate the recorded radiation field to a corresponding temperature field and, thus, provides an easy-to-use alternative for real-time monitoring of melt pool surface temperature [31]. However, the use of a single emissivity-based conversion factor for the temperature field of the entire melt pool and adjacent trailing solidified region can be erroneous as emissivity of metallic surfaces is a function of temperature [31]. An attempt is therefore presented here to provide a comparison of the recorded temperature field from the two-colour and mono-colour thermal camera, which can illustrate the likely error in measurement when using an easy-to-use mono-colour camera compared to a two-colour camera that is relatively costly and requires complex setting. A single emissivity-based conversion factor of ~0.85 is used in this work to calibrate the temperature field from the mono-colour cameras [31]. Figure 3g–i and j–l show the recorded temperature field for unidirectional and bidirectional scanning strategies, respectively, from the mono-colour camera. A comparison between Fig. 3a–c and Fig. 3g–i shows that recorded temperature fields from both the two-colour and

mono-colour cameras for the second, sixth, and ninth layers are fairly similar for unidirectional scanning. The melt pool sizes recorded from the mono-colour camera in Fig. 3g–i are slightly larger than the same recorded from the two-colour camera in Fig. 3a–c for unidirectional deposition. A similar trend of melt pool temperature field and corresponding sizes is also noted for all the layers for bidirectional scanning, as indicated in Fig. 3d–f and j–l. A maximum deviation of around ±2 mm for the melt pool length and ±10% for the peak temperature is noted between the processed images from the mono-colour and two-colour thermal cameras. A more deterministic approach to obtain the melt pool length from the recorded temperature field is illustrated further in Fig. 4.

Figure 4a–b present the variation of temperature along the centreline (line AB in Fig. 4c) of layer surfaces, corresponding to an instant when the arc centre is at point A, for unidirectional and bidirectional scanning. The temperature contours in Fig. 4a–b are extracted from the recorded temperature field by the two-colour camera. Figure 4a–b provide a way to measure the average melt pool length for each layer by considering the intersection of the instantaneous temperature contour and the liquidus temperature (1812 K) line. An increase in the melt pool length from the bottom to the top layers can be noted in both Fig. 4a and b, which is attributed to the increase in the overall build temperature and reducing heat loss rate through the build height as deposition moves to upper layers. A comparison of Fig. 4a and b shows that the increase in the melt pool length from the first to the ninth

Fig. 4 Measured temperature contours along the deposition centreline (line AB in **c**) from two-colour camera (TC) for the first, third, fifth, seventh, and ninth layers for **a** unidirectional and **b** bidirectional scanning
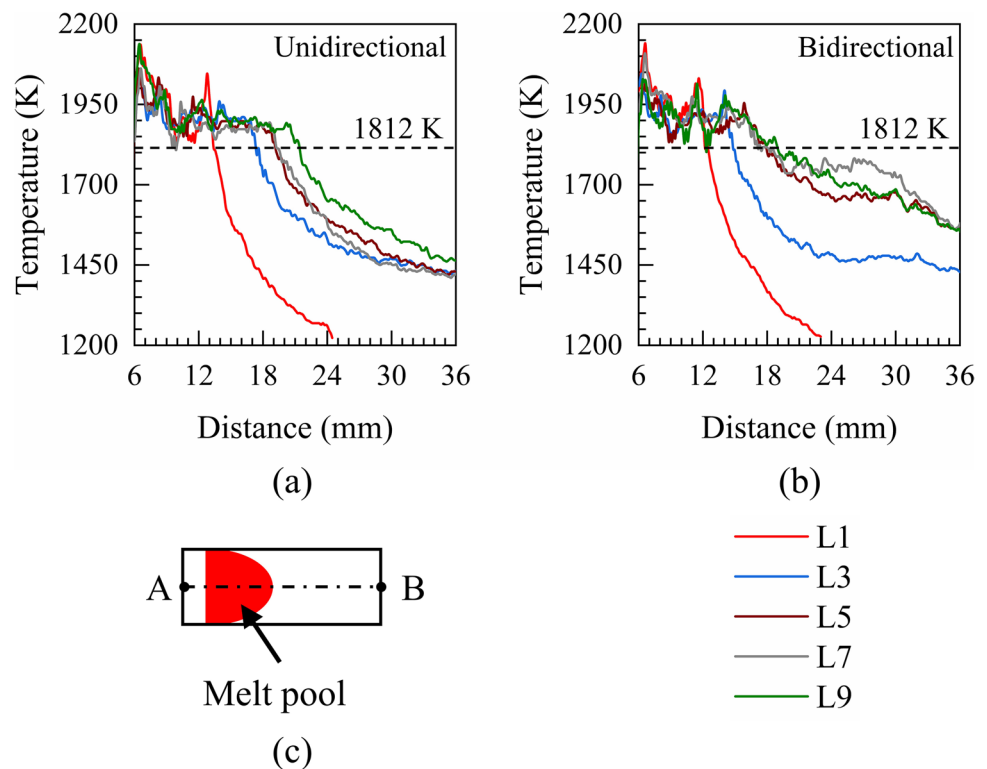
layer is around 8 mm and 6 mm for the unidirectional and bidirectional scanning, respectively.

3.3 Estimation of thermal cycle and cooling rate

The layer-wise thermal cycle and solidification cooling rate can provide an assessment of the structure and properties of the builds in GMA-DED [14, 15]. The thermal cycles are monitored at the middle of the track (at point P in Fig. 5c) using the sliding frame analysis of the temperature field, which is recorded from the two-colour camera. Figure 5a–b present the calculated thermal cycles for the deposition of odd layers for both unidirectional and bidirectional scanning. The thermal cycles are not plotted for all the layers in Fig. 5a–b to avoid crowing of several contours and maintain clarity. The cooling rate ($\dot{T}$) at solidification is calculated further from the thermal cycles at five adjacent points near the mid-length of the deposited layers as

$$\dot{T} = \frac{T_L - T_S}{\Delta t} \tag{1}$$

where T_L is the liquidus temperature (1812 K), T_S is the solidus temperature (1758 K) [32], and Δt is the time interval

to cool down from the liquidus to solidus temperature at a specific point, respectively.

The computed cooling rates ($\dot{T}$) at solidification reduce remarkably from 1346 K/s for the first layer to 750 K/s for the third layer followed by a gentle decrease through the fifth, seventh, and ninth layers as 720 K/s, 610 K/s, and 509 K/s, respectively, for the unidirectional scanning. In contrast, the computed cooling rates ($\dot{T}$) at solidification for the bidirectional scanning reduce from 1317 K/s for the first layer to 425 K/s for the third layer followed by 394 K/s, 292 K/s, and 177 K/s for the fifth, seventh, and ninth layers, respectively. The decrease in the cooling rates ($\dot{T}$) at solidification from the first to the ninth layer is attributed to an increase in the time interval Δt in the upper layers as the heat accumulation of the build increases and the rate of heat loss reduces through the already solidified layers reduces.

3.4 Measurement of melt pool dimensions

Figure 6a–b present the measured melt pool dimensions along different layers for the unidirectional scanning. The melt pool depth and length are obtained from the longitudinal (x-z) sectional view of the pool (Fig. 6c), which is recorded by the high-speed video camera. The melt pool width is monitored from the top surface temperature field

Fig. 5 Calculated thermal cycles at the mid-length (point P in **c**) along the deposited surfaces of the first, third, fifth, seventh, and ninth layers for **a** unidirectional and **b** bidirectional scanning. These thermal cycles are calculated from the surface temperature field recorded by the two-colour camera
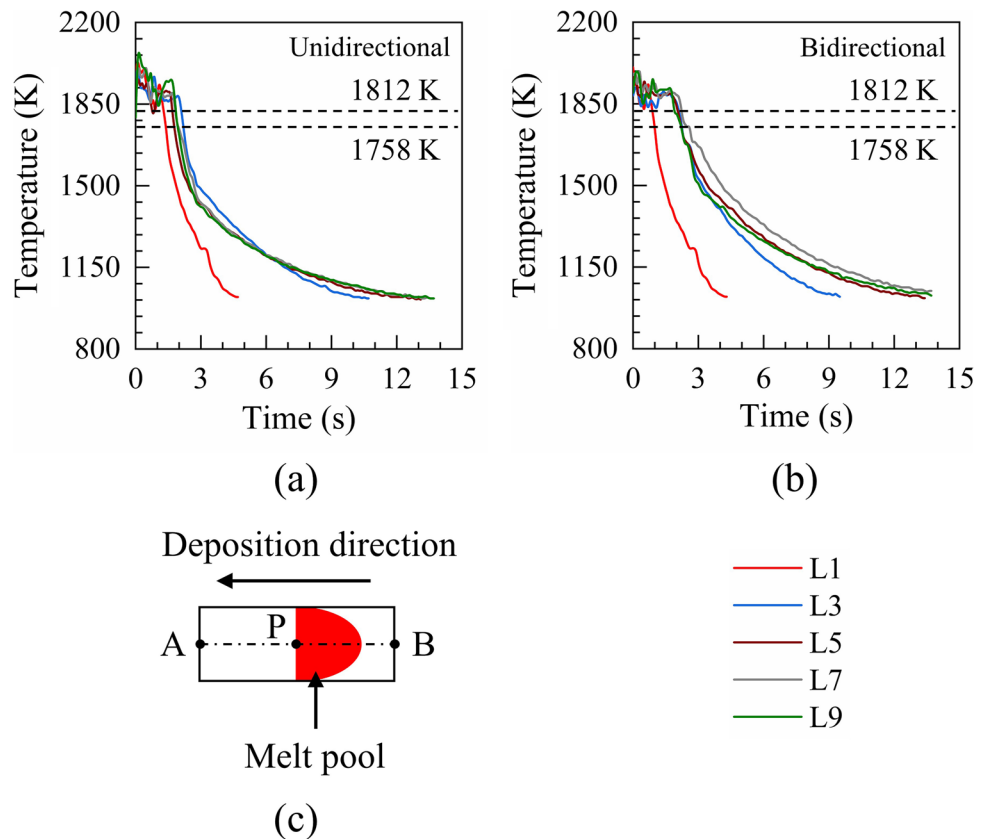
(Fig. 6c), which is recorded by the two-colour camera. The melt pool width shows little increase from the first to the fourth layer and seizes to grow further in the upper layers (Fig. 6a). The average melt pool depth increases with the number of layers and attains nearly a plateau after the seventh layer (Fig. 6a). The average melt pool length increases continuously from the first to the seventh layer (Fig. 6b). It can be noted that the video camera could not capture the entire pool length beyond the seventh layer as the melt pool moved out of the pre-set region of interest (ROI).

A similar analysis of the measured melt pool dimensions for the bidirectional scanning has also showed that the pool depth and width increase gently from the first to around the fourth layer and remain almost unchanged for the upper layers [7]. The melt pool length also increases for upper layers during bidirectional scanning similar to that observed in unidirectional scanning. For a given heat input, the average melt pool length along a layer is found to be ever larger for unidirectional scanning in comparison to that for the bidirectional scanning. In contrast, the melt pool depth and width are usually found to be slightly greater for bidirectional scanning in comparison to that in unidirectional scanning.

3.5 Measurement of build profiles and hardness

An attempt is made further to examine the consistency of build dimension and properties such as microhardness along

the deposited height at various transverse cross-sections which are prepared from multi-layer walls with unidirectional and bidirectional scanning. Figure 7a–b show the as-deposited ten-layer walls with unidirectional and bidirectional scanning, respectively. The measured wall heights at the start and end of the deposition are respectively 33.9 and 17.4 mm for unidirectional scanning (Fig. 7a). The greater wall height at the starting position is attributed to fast freezing of the melt pool, which inhibits its flow [4]. The inclination of the deposited layer with the x-axis (θ_2) is measured along the ninth layer to check the consistency of the real-time measured result from high-speed images (Fig. 2b). The measured inclination (θ_1) from the build cross-section is around 16.05° (± 0.25) (Fig. 7a) and that from the high-speed image is around 15.91° (± 0.25) (Fig. 2b), which are in fair agreement and show the efficacy of the real-time monitoring for GMA-DED.

Figure 7c–g show the transverse cross-sections of the ten-layer wall along the sections A-A, B-B, and C-C for the unidirectional scanning, and along the sections D-D and E-E for the bidirectional scanning, respectively. The measured height and the maximum width of each ten-layer wall cross-sections are also shown in Fig. 7c–g. For unidirectional scanning, the height of the deposited wall reduces continuously from the start-point to the end-point as observed in Fig. 7c–e. In contrast, the bidirectional scanning has yielded little variations in the wall height along the length of the deposit (Fig. 7b, f–g). The wall width


Fig. 6 Measured melt pool **a** depth and width, and **b** length for unidirectional scanning, and **c** illustration for the measurement of melt pool dimensions
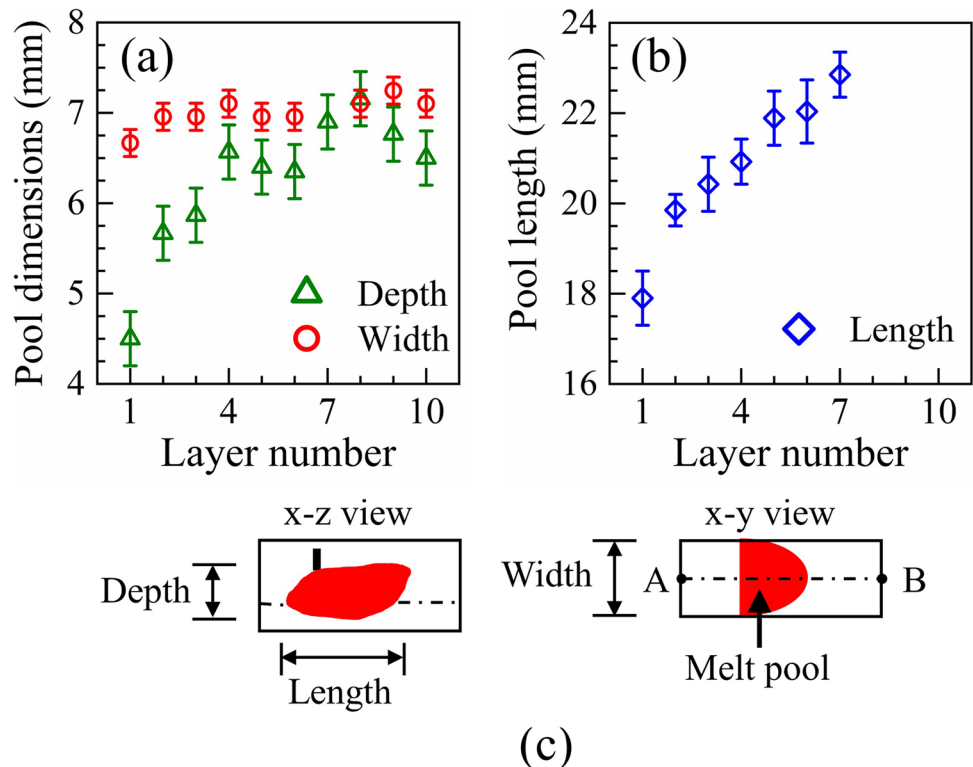
for unidirectional scanning also varies from 8.7 mm at the start-point to 6.9 mm at the mid-length and around 7.1 mm at the end-point, but the bidirectional scanning has provided a fairly consistent wall width along the length of the deposit. Overall, shows that the bidirectional scanning can produce a fairly consistent multi-layer wall in comparison to unidirectional scanning.

The nature of diversity in the wall width through the height of the deposited ten-layer wall is examined further for a quantitative understanding. Figure 8 shows measured wall widths through the height of the ten-layer walls along the sections A-A, B-B, and C-C (Fig. 7) for unidirectional scanning and along the sections D-D and E-E (Fig. 7) for bidirectional scanning. For each cross-section, the wall width has been measured at around 15 to 20 equally spaced points and around each monitoring point, three to five measurements are made to obtain the variability, which is shown as error

bars in Fig. 8. The measured wall widths are found to gently increase towards the upper layers, which is expected due to heat accumulation in the deposited layers and reduced rate of heat loss through these layers. A slightly smaller width is observed along the top surface, which is attributed to the parabolic profile of the last deposited layer. The average wall widths along the sections A-A, B-B, and C-C for unidirectional scanning are around 8.1 mm, 6.2 mm, and 6.9 mm, respectively, with the corresponding deviations of around 4%, 7%, and 4%. In contrast, the average wall widths along the sections D-D and E-E for bidirectional scanning are 7.1 mm and 7.4 mm, respectively, with the corresponding deviations of around 4% in both the cases. A comparison of the measured melt pool width by the thermal cameras in Fig. 6a and the corresponding measured wall width in Fig. 8 shows the maximum deviation in the range of around ± 0.82 mm.
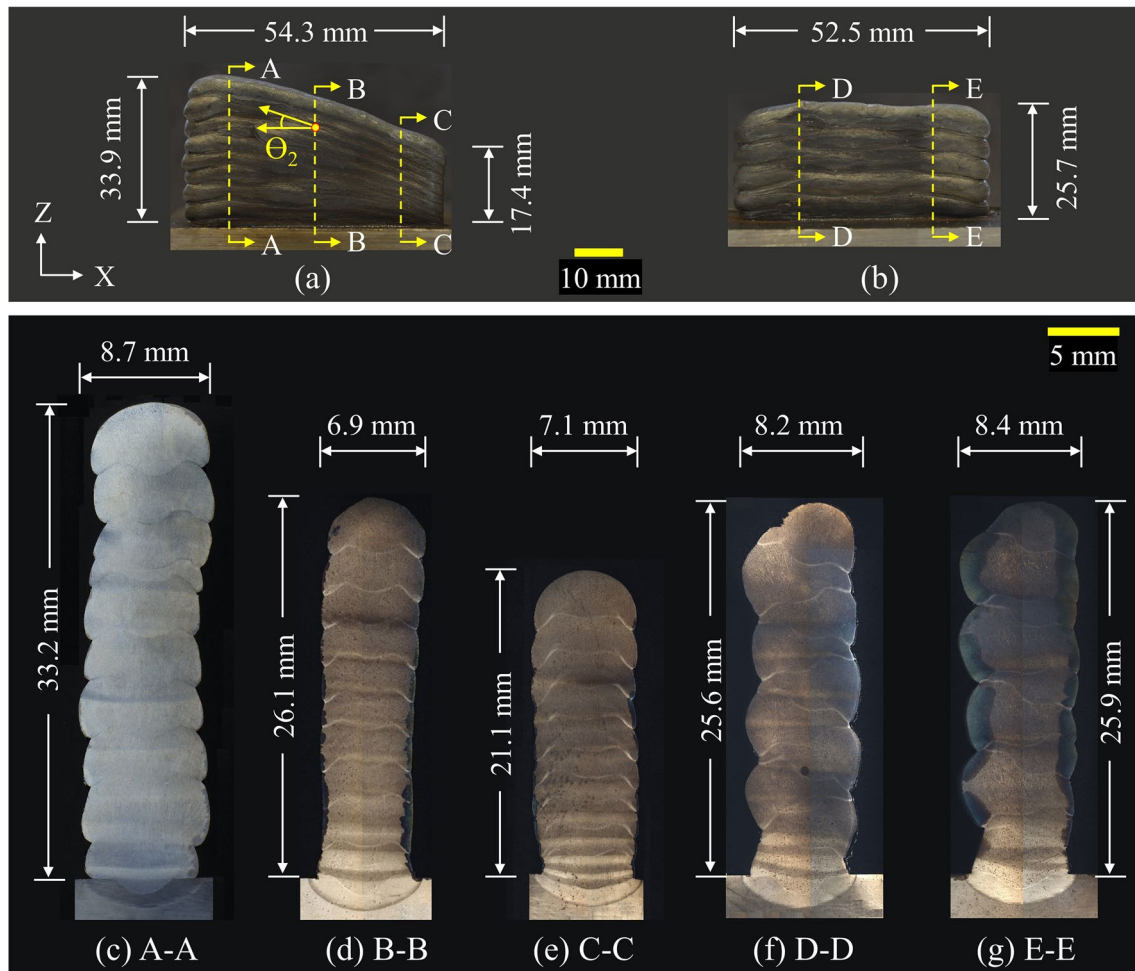
Fig. 7 **a–b** Ten-layer wall deposits for **a** unidirectional and **b** bidirectional scanning. For unidirectional scanning, three transverse sections along the length such as **c** A-A (start), **d** B-B (mid-length), and **e** C-C (end) are shown. For bidirectional scanning, two transverse sections along the length such as **f** D-D (between start and mid-length) and **g** E-E (between mid-length and end) are shown. The inclination angle θ_2 in the deposition direction (*x*-axis) is measured along the ninth layer
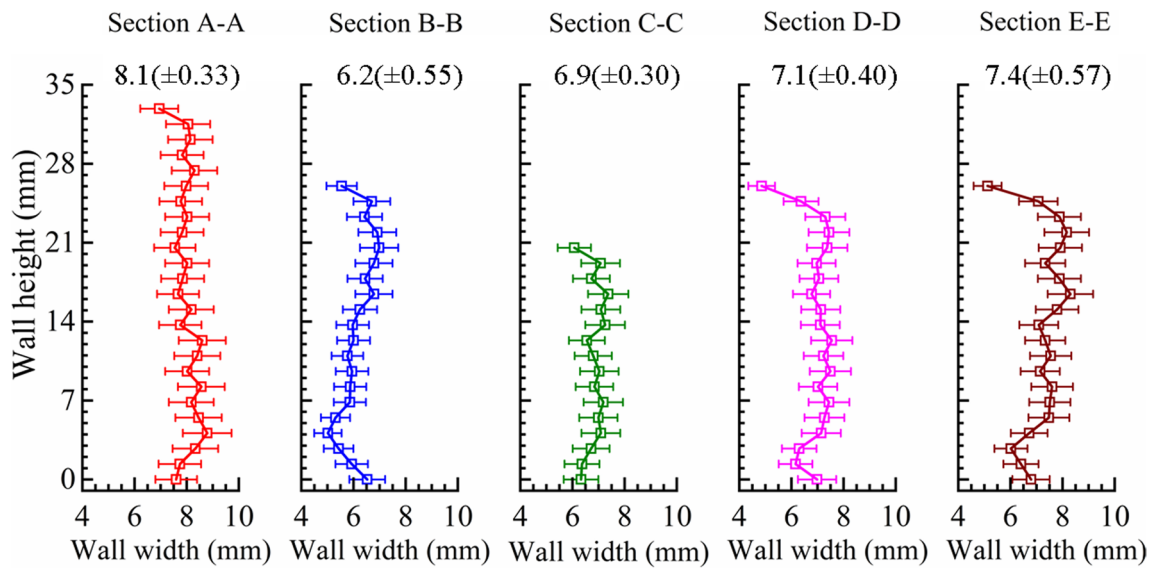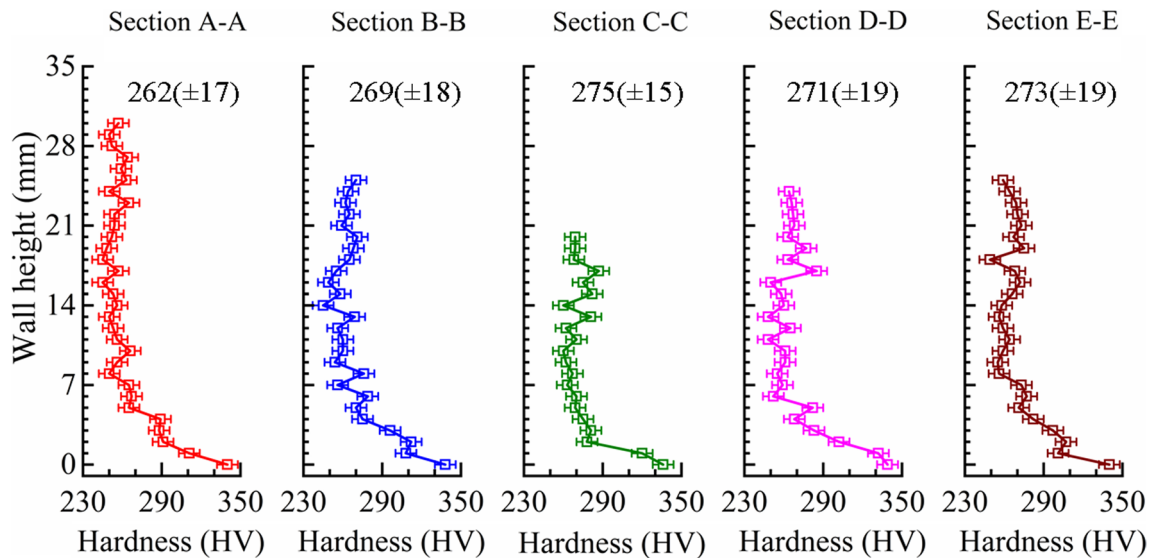
Fig. 8 Variation in the measured wall width through the height along three sections (A-A, B-B, C-C, Fig. 7) for unidirectional scanning and along two sections (D-D, E-E, Fig. 7) for bidirectional scanning. The open square symbols represent the measuring locations

The variations in wall width through the height of the wall along different sections of the deposited multi-layer wall manifest a need to also examine the uniformity of inherent mechanical property such as microhardness through the wall heights. Figure 9 illustrates the measured microhardness through the wall heights along the sections A-A, B-B, and C-C (Fig. 7) for unidirectional scanning and along the sections D-D and E-E (Fig. 7) for bidirectional scanning. The measured hardness is always higher near the substrate, which is attributed to a harder structure due to rapid heat dissipation through the substrate and high cooling rate. As the heat dissipation rate reduces and the cooling rate slows down in the upper layers, the layer hardness reduces and becomes nearly uniform. The average measured microhardness of the sections A-A, B-B, and C-C for the unidirectional scanning are around 262 ($\pm$17) HV, 269 ($\pm$18) HV, and 275 ($\pm$15) HV, respectively. In contrast, the average measured microhardness of both the sections D-D and E-E for the bidirectional scanning are around 272 ($\pm$19) HV. Overall, Fig. 9 exhibits that the bidirectional scanning can result in more uniform mechanical properties through the length of the deposited multi-layer wall.

Fig. 9 Variation in the measured hardness through the wall height along three sections (A-A, B-B, C-C, Fig. 7) for unidirectional scanning and along two sections (D-D, E-E, Fig. 7) for bidirectional scanning. The open square symbols represent the measuring locations

4 Summary and conclusions

A novel experimental investigation is presented for the synchronous real-time monitoring of metal transfer, longitudinal and top view of melt pool, and arc power for GMA-DED for multi-layer wall depositions with unidirectional and bidirectional scanning. A video camera is used to monitor the metal transfer and melt pool longitudinal section at a high sampling rate of around 2.6 kHz. The temperature field of the melt pool and adjoining trailing solidified region is captured in real-time by thermal cameras. The recorded process transients are analysed to extract the dimensions of melt pool, thermal cycles, and cooling rate at solidification along the layers. Following are the main conclusions.

- The synchronous monitoring of current and voltage transients, dynamic metal transfer, and melt pool surface temperature provides an integrated framework to assess the dimensional consistency of the multi-layer depositions during GMA-DED.
- For a given heat input and scanning strategy, the melt pool dimension increase and the cooling rate at solidification decreases towards the upper layers, which is attributed to the retarding rate of heat loss through the solidified layers at elevated temperature. The nature of these diversity is observed to be relatively larger for unidirectional scanning.
- The bidirectional scanning yielded a more consistent dimension and microhardness through the multi-layer wall deposits in comparison to unidirectional scanning for GMA-DED.

Declarations

References

1. Williams SW, Martina F, Addison AC, Ding J, Pardal G, Colegrove P (2016) Wire+arc additive manufacturing. Mater Sci Technol 32:641–647. https://doi.org/10.1179/1743284715Y.0000000073
2. Wu B, Pan Z, Chen G, Ding DH, Yuan L, Cuiuri D, Li HJ (2019) Mitigation of thermal distortion in wire arc additively manufactured Ti6Al4V part using active interpass cooling. Sci Technol Weld Joining 24:484–494. https://doi.org/10.1080/13621718.2019.1580439
3. DebRoy T, Wei HL, Zuback JS, Mukherjee T, Elmer JW, Milewski JO, Beese AM, Wilson-Heid A, De A, Zhang W (2018) Additive manufacturing of metallic components — process, structure and properties. Prog Mater Sci 92:112–224. https://doi.org/10.1016/j.pmatsci.2017.10.001
4. Ogino Y, Asai S, Hirata Y (2018) Numerical simulation of WAAM process by a GMAW weld pool model. Weld World 62:393–401. https://doi.org/10.1007/s40194-018-0556-z
5. Rodrigues TA, Duarte V, Avila JA, Santos TG, Miranda RM, Oliveira JP (2019) Wire and arc additive manufacturing of HSLA steel: effect of thermal cycles on microstructure and mechanical properties. Addit Manuf 27:440–450. https://doi.org/10.1016/j.addma.2019.03.029
6. Yang D, Wang G, Zhang G (2017) Thermal analysis for single-pass multi-layer GMAW based additive manufacturing using infrared thermography. J Mater Process Technol 244:215–224. https://doi.org/10.1016/j.jmatprotec.2017.01.024
7. Chaurasia PK, Goecke SF, De A (2022) Real-time monitoring of temperature field, metal transfer and cooling rate during gas metal arc-directed energy deposition. Sci Technol Weld Joining 27:512–521. https://doi.org/10.1080/13621718.2022.2080447
8. Chaurasia PK, Goecke SF, De A (2023) Monitoring melt pool asymmetry in gas metal arc-directed energy deposition. Sci Technol Weld Joining. https://doi.org/10.1080/13621718.2023.2168933
9. Makwana P, Goecke SF, De A (2019) Real-time heat input monitoring towards robust GMA brazing. Sci Technol Weld Joining 24:16–26. https://doi.org/10.1080/13621718.2018.1470290
10. Nagarajan S, Banerjee P, Chen WH, Chin BA (1992) Control of welding process using infrared sensors. IEEE Trans Rob Autom 8:86–93. https://doi.org/10.1109/70.127242
11. Chin BA, Madsen NH, Goodling JS (1983) Infrared thermography for sensing the arc welding process. Weld J 62:227–234
12. Su C, Chen X (2019) Effect of depositing torch angle on the first layer of wire arc additive manufacturing using cold metal transfer (CMT). Ind Robot 42:259–266. https://doi.org/10.1108/IR-11-2018-0233
13. Wang W, Wang Z, Hu S, Bai P, Lu T, Cao Y (2018) Weld pool surface fluctuations sensing in pulsed GMAW. Weld J 97:327S–337S. https://doi.org/10.29391/2018.97.028
14. Nair AM, Muvvala G, Sarkar S, Nath AK (2020) Real-time detection of cooling rate using pyrometers in tandem in laser material processing and directed energy deposition. Mater Lett 277:128330. https://doi.org/10.1016/j.matlet.2020.128330
15. Mathieu A, Mattei S, Deschamps A, Martin B, Grevey D (2006) Temperature control in laser brazing of a steel/aluminium assembly using thermographic measurements. NDT E Int 39:272–276. https://doi.org/10.1016/j.ndteint.2005.08.005
16. Hooper PA (2018) Melt pool temperature and cooling rates in laser powder bed fusion. Addit Manuf 22:548–559. https://doi.org/10.1016/j.addma.2018.05.032
17. Yamazaki K, Yamamoto E, Suzuki K, Koshiishi F, Waki K, Tashiro S (2010) The measurement of metal droplet temperature in GMA welding by infrared two-colour pyrometry. Weld Int 24:81–87. https://doi.org/10.1080/09507110902842950
18. Yamazaki K, Yamamoto E, Suzuki K, Koshiishi F, Tashiro S, Tanaka M, Nakata K (2010) Measurement of surface temperature of weld pools by infrared two colour pyrometry. Sci Technol Weld Joining 15:40–47. https://doi.org/10.1179/136217109X12537145658814
19. Yamada J, Murase T, Kurosaki Y (2003) Thermal imaging system applying two-color thermometry. Heat Transfer Asian Res 32:473–488. https://doi.org/10.1002/htj.10104
20. Gao XS, Wu CS, Goecke SF, Kuegler H (2017) Effects of process parameters on weld bead defects in oscillating laser-GMA hybrid welding of lap joints. Int J Adv Manuf Technol 93:1877–1892. https://doi.org/10.1007/s00170-017-0637-y

21. Hermans MJM, Den Ouden G (1999) Process behavior and stability in short circuit gas metal arc welding. Weld J 78:137S–141S

22. Ersoy U, Hu SJ, Kannatey-Asibu E (2008) Observation of arc start instability and spatter generation in GMAW. Weld J 87:51S–56S

23. Dos Santos EBF, Pistor R, Gerlich AP (2017) Pulse profile and metal transfer in pulsed gas metal arc welding: droplet formation, detachment and velocity. Sci Technol Weld Joining 22:627–641. https://doi.org/10.1080/13621718.2017.1288889

24. Johnson JA, Carlson NM, Smartt HB, Clark DE (1991) Process control of GMAW: sensing of metal transfer mode. Weld J 70:91–99

25. Zou S, Wang Z, Hu S, Zhao G, Wang W, Chen Y (2020) Effects of filler wire intervention on gas tungsten arc: part II — dynamic behaviors of liquid droplets. Weld J 99:271S–279S. https://doi.org/10.29391/2020.99.025

26. Wu BT, Ding DH, Pan ZX, Cuiuri D, Li HJ, Han J, Fei ZY (2017) Effects of heat accumulation on the arc characteristics and metal transfer behavior in wire arc additive manufacturing of Ti6Al4V. J Mater Process Technol 250:304–312. https://doi.org/10.1016/j.jmatprotec.2017.07.037

27. Wang YM, Zhang CR, Lu J, Bai LF, Zhao Z, Han J (2020) Weld reinforcement analysis based on long-term prediction of molten pool image in additive manufacturing. IEEE Access 8:69908–69918. https://doi.org/10.1109/ACCESS.2020.2986130

28. Cadiou S, Courtois M, Carin M, Berckmans W, Le Masson P (2020) 3D heat transfer, fluid flow and electromagnetic model for cold metal transfer wire arc additive manufacturing (Cmt-Waam). Addit Manuf 36:101541. https://doi.org/10.1016/j.addma.2020.101541

29. Mezrag B, Beaume FD, Rouquette S, Benachour M (2018) Indirect approaches for estimating the efficiency of cold metal transfer welding process. Sci Technol Weld Joining 23:508–519. https://doi.org/10.1080/13621718.2017.1417806

30. Pepe N, Egerland S, Colegrove PA, Yapp D, Leonhartsberger A, Scotti A (2011) Measuring the process efficiency of controlled gas metal arc welding processes. Sci Technol Weld Joining 16:412–417. https://doi.org/10.1179/1362171810Y.0000000029

31. Optris infrared thermometers: 'basic principles of noncontact temperature measurements' http://www.optris.co.uk/thermal-imager-optris-pi-m?file=tl_files/pdf/Downloads/Zubehoer/IR-Basics.pdf

32. Goecke S-F, Goett G, Sikstroem F (2017) Comparison and validation of different thermographic methods in steel welding. 70th IIW Annual Assembly and International Conference Doc. SG212-1494-17/XII-2346-17/ IV-1348-17/I-1331-17